Journal of Alloys and Compounds 1020 (2025) 179353

Contents lists available at ScienceDirect

Journal of Alloys and Compounds

journal homepage: www.elsevier.com/locate/jalcom

Optimized hydrogen-supplying gate insulator for high-mobility indium oxide TFTs via atomic-level oxygen reactant engineering

Hwa Young Kim [a], Seong-In Cho [a,b,c], Dong Yeob Shin [d], Kwun-Bum Chung [d], Sang-Hee Ko Park [a], Jong Beom Ko [e,*]

[a] Department of Materials Science and Engineering, Korea Advanced Institute of Science and Technology (KAIST), Yuseong-gu, Daejeon 34141, Republic of Korea
[b] Inter-University Semiconductor Research Center (ISRC), Seoul National University, Seoul 08826, Republic of Korea
[c] Department of Electrical and Computer Engineering, Seoul National University, Seoul 08826, Republic of Korea
[d] Department of Physics and Semiconductor Science, Dongguk University, Seoul 04620, Republic of Korea
[e] Department of Materials Science and Engineering, Hanbat National University, Yuseong-gu, Daejeon 34158, Republic of Korea

ARTICLE INFO

Keywords:
Indium oxide thin-film transistor (In_2O_3 TFT)
Atomic layer deposition (ALD)
Super-cycle
Aluminum oxide (Al_2O_3)
Hydrogen control

ABSTRACT

Oxide thin-film transistors (TFTs) have garnered significant interest owing to their potential in advanced electronic applications. The performance of these devices can be positively or negatively modulated by hydrogen doping into oxide semiconductor, with atomic layer deposited gate insulators (GIs) serving as a key method. This study introduces a novel method of oxygen reactant engineering for the atomic layer deposition (ALD) of GI, specifically aimed at fabricating In_2O_3 TFTs using a super-cycle-deposited Al_2O_3 to effectively control the amount of hydrogen incorporation. Although In_2O_3 was selected as the channel layer for its exceptionally high mobility, it required further optimization due to its variable carrier concentration and numerous defects such as oxygen vacancies and interstitials. By alternately using H_2O and O_2 plasma as oxygen reactants in the deposition of Al_2O_3 GIs, we achieved precise modulation of hydrogen levels and simultaneously passivated the defects while managing the carrier concentration in In_2O_3. With appropriate hydrogen incorporation, the device exhibited a superior performance including a mobility of 148.1 cm^2/Vs and a turn on voltage (V_{on}) of −0.85 V. The devices with either excessive or insufficient hydrogen demonstrated shifts in V_{on} and stability issues. Through various analyses, we confirmed that a specific level of hydrogen penetration passivated oxygen-related defects, while further hydrogen diffusion substantially increased the carrier concentration. This study reports the effectiveness of the oxygen reactant engineering in ALD for precise hydrogen control and optimization of electronic properties in oxide semiconductors for application in advanced TFTs.

1. Introduction

In recent years, oxide semiconductors have become integral to various electronic applications, including field-effect transistors, memory devices, and sensors [1–3]. Their superior electrical properties, low thermal budgets, and uniformity across large areas render them essential for advanced electronic technologies. These materials show remarkable promise as channel layers in thin-film transistors (TFTs), which have been extensively studied for applications in display and semiconductor devices. To improve the performance of oxide TFTs, significant research has focused on multicomponent oxide materials, novel TFT structures, and semiconductor crystallization [4–6]. The increasing demand for high-resolution displays and innovative technologies highlights the significance of oxide semiconductors. Indium oxide (In_2O_3) is an oxide semiconductor characterized by exceptionally high mobility, which originates from spherical orbital overlap and low effective electron mass, facilitating electron transport [7,8]. However, its extremely high carrier concentration and numerous defects pose challenges for its standalone application [9,10]. Efforts to incorporate dopants such as gallium oxide (Ga_2O_3), zinc oxide (ZnO), and fluorine (F) into In_2O_3 have typically resulted in significant reduction in mobility [11–13]. Consequently, research has shifted toward the use of pure In_2O_3, typically achieved via sputtering deposition [10,14]. Unfortunately, sputtering-induced atomic collisions introduced several defects and complicated the fine control of thickness and composition. Atomic layer deposition (ALD) has emerged as a promising solution to these

* Corresponding author.
E-mail address: jko914@hanbat.ac.kr (J.B. Ko).

https://doi.org/10.1016/j.jallcom.2025.179353
Received 8 November 2024; Received in revised form 3 February 2025; Accepted 21 February 2025
Available online 21 February 2025

challenges. The self-limiting surface reactions in ALD enable the deposition of atomic monolayers [15], allowing for precise thickness control, improved step coverage, and high film quality. Furthermore, the super-cycle approach in ALD facilitates precise modulation of film composition by adjusting the number of subcycles for materials such as InGaZnO (IGZO), InSnZnO (ITZO) and InAlZnO (IAZO) [16–18]. Through these methods, significant enhancements in the electrical properties of oxide semiconductors have been achieved. Nevertheless, attaining a mobility exceeding 100 cm^2/Vs remains challenging, which positions In_2O_3 with its large 5 *s* orbital as a promising candidate to overcome this limitation.

The top-gate configuration is increasingly favored for high-end devices among various TFT structures [19,20]. However, the direct deposition of a gate insulator (GI) on the semiconductor can adversely affect the underlying layer and overall device performance. Furthermore, hydrogen incorporation during the GI process or its diffusion from the GI into the active layer is unavoidable during high-temperature post-processing. Although hydrogen can passivate the electron trap sites and enhance TFT stability [21,22], excessive hydrogen can significantly increase the carrier concentration [23,24], presenting a challenge in controlling hydrogen penetration. Consequently, various methods such as hydrogen annealing, plasma treatment, and the implementation of hydrogen barriers and injection layers have been explored [25–28]. Conventional SiO_2 GIs often encounter issues with gate leakage currents, which lead to a deterioration of TFT performance. Aluminum oxide (Al_2O_3) has emerged as a superior alternative owing to its high dielectric constant, low leakage current, and excellent barrier properties [29]. Al_2O_3, when deposited by ALD, also enhances the film quality and reduces the number of electron trap sites [30,31]. Al_2O_3 can be deposited using thermal ALD (T-ALD) and plasma-enhanced ALD (PEALD). T-ALD-deposited Al_2O_3 (T-Al_2O_3) using H_2O as an oxygen reactant introduces a significant amount of hydrogen into the channel layer during the process, which degrades TFT performance; however, reliance on thermal energy reduces damage from external source such as plasma, making it advantageous for maintaining a stable interface. In contrast, PEALD-deposited Al_2O_3 (PE-Al_2O_3) contains low hydrogen impurities and exhibits high density; however, it may introduce charge trapping defects (e.g., M-O-O) within the active layer due to oxygen plasma exposure [32].

This study introduces a novel super-cycle ALD method that combines PE-Al_2O_3 and T-Al_2O_3 to regulate both the hydrogen concentration in the GI and the plasma-induced defects within the active layer and the interface between active layer and GI. Unlike previous super-cycle studies that primarily focused on multicomponent oxides [16–18], this study employs two different oxygen reactants (H_2O and O_2 plasma) in the super-cycle. This approach is designed to advance the insulator to complement semiconductor research on well-behaved TFTs. We assessed the hydrogen incorporation and electrical characteristics of the TFTs by depositing Al_2O_3 using the super-cycle method and conducting advanced hydrogen-related advanced analyses. We successfully fabricated an extraordinarily high-mobility In_2O_3 top-gate TFT with an optimal hydrogen concentration by adjusting the subcyclic ratio of the Al_2O_3 GIs.

2. Experimental section

2.1. Fabrication of In_2O_3 TFTs

We fabricated TFTs with a top-gate bottom-contact (TGBC) structure, as depicted in Fig. 1(a). This structure involves the deposition of a GI directly atop the active layer, which allows us to explore the intricate effects of the GI on the semiconductor properties and optimization of their interface. The fabrication process started with the formation of source/drain (S/D) electrodes on a glass substrate, achieved by patterning 150-nm-thick sputtered InSnO (ITO). Subsequently, a 5-nm-thick In_2O_3 was deposited as the active layer at 200 °C using PEALD. The deposition utilized [3-(dimethylamino)propyl]dimethylindium (DADI) as the indium precursor, with 100 W RF O_2 plasma as the oxygen

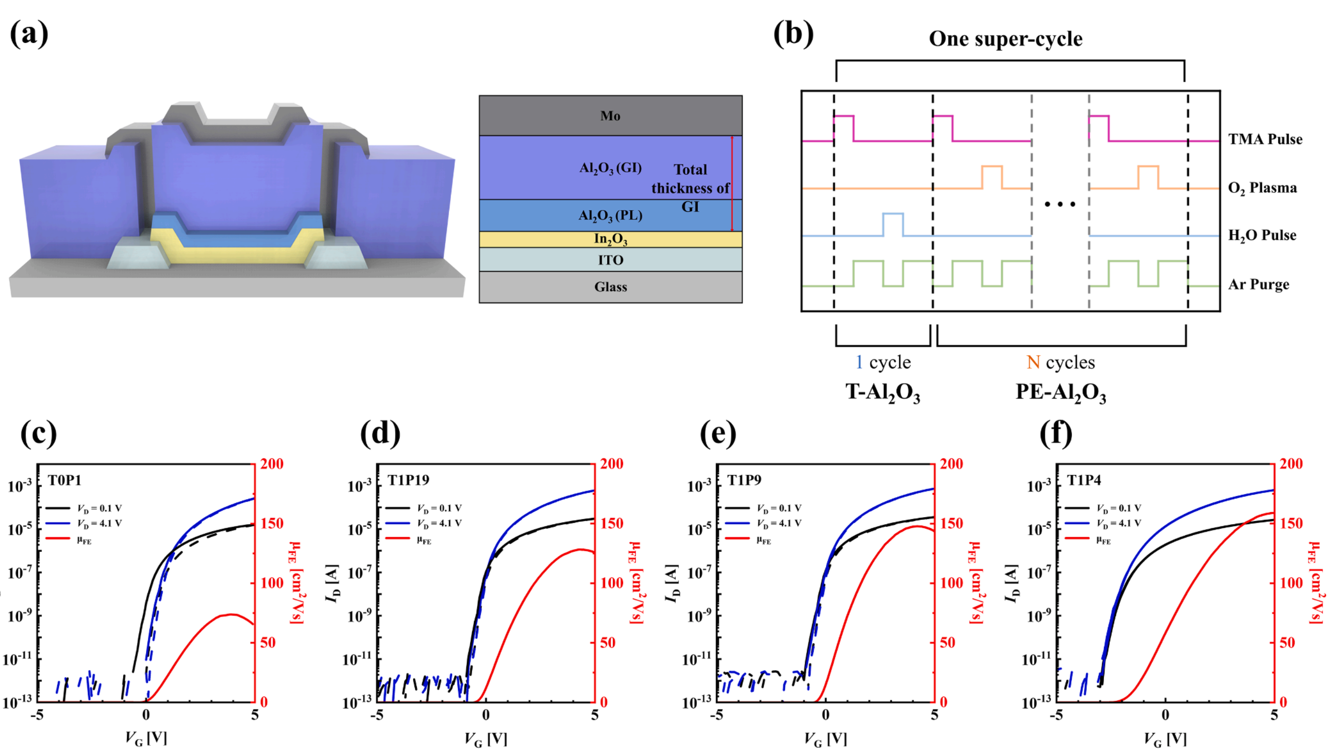

Fig. 1. Schematic of (a) TGBC TFT and its constituent layer, and (b) representation of one super-cycle during Al_2O_3 deposition. Transfer characteristics of (c) T0P1, (d) T1P19, (e) T1P9, and (f) T1P4 devices. Solid and dashed lines in black and blue correspond to drain current during forward and reverse gate voltage sweeps, respectively.

reactant. The DADI precursor was maintained at 40 °C within the delivery cylinder, and the deposition process was performed under a chamber pressure below 1 Torr. Each deposition cycle comprised the following sequence: (1) DADI precursor dose for 1.0 s with an Ar carrier gas flow rate of 50 sccm, (2) Ar purge for 10 s, (3) 2.0 s exposure to 100 W RF O_2 plasma with an oxygen gas flow rate of 500 sccm, and (4) Ar purge for 10 s. To mitigate intrinsic oxygen-related defects in In_2O_3, the surface underwent an O_2 plasma treatment at 130 W for 540 s at 200 °C. Following this, a 10 nm-thick Al_2O_3 protection layer (PL) was deposited in-situ over the In_2O_3 to shield it from chemical exposure during subsequent patterning [33]; this layer was patterned simultaneously with the active layer. An additional 20 nm of Al_2O_3 was then deposited to form the main GI. Both the PL and the main GI were deposited using a super-cycle method combining of T-ALD and PEALD, detailed in Section 2.2. The total effective thickness of the GI, combining both the PL and main GI, operated as 30 nm as shown in Fig. 1(a). Contact holes were then created to expose the S/D electrodes, followed by the deposition of an 80-nm-thick Mo layer through DC sputtering at room temperature, which was patterned to form the gate electrode. All patterning was performed using photolithography and wet chemical techniques, and the devices were vacuum annealed at 310 °C for 3 h for post-treatment. The completed devices featured channel widths and lengths of 20 and 10 μm, respectively.

2.2. Deposition of Al_2O_3 films using super-cycle method

Regarding the deposition of Al_2O_3, T-ALD employs H_2O as the oxygen reactant, whereas PEALD employs O_2 plasma. The Al_2O_3 films were alternately deposited using the super-cycle method, as illustrated in Fig. 1(b). The subcyclic ratios of T-Al_2O_3 to PE-Al_2O_3 were adjusted to 1:4, 1:9 and 1:19, with a pristine PE-Al_2O_3 film serving as a reference. These configurations were designated T1P4, T1P9, T1P19, and T0P1 (PE-Al_2O_3 only), corresponding to T-Al_2O_3 proportions of 20 %, 10 %, 5 %, and 0 % of the total layer, respectively. The Al_2O_3 films were deposited using trimethylaluminum (TMA) as the aluminum precursor at a substrate temperature of 200 °C. Both TMA and H_2O precursors were maintained at ambient temperature in the cylinder, and the deposition was performed under a chamber pressure below 1 Torr. The T-Al_2O_3 deposition process entitled the following steps: (1) TMA dose for 0.2 s with an Ar carrier gas flow rate of 500 sccm, (2) Ar purge for 5.0 s, (3) H_2O dose for 0.3 s with an Ar carrier gas flow rate of 500 sccm, and (4) Ar purge for 7.0 s. In contrast, the PE-Al_2O_3 deposition process proceeded as follows: (1) TMA dose for 0.2 s with an Ar carrier gas flow rate of 500 sccm, (2) Ar purge for 5.0 s, (3) RF O_2 plasma exposure at 100 W for 2.0 s with an oxygen gas flow rate of 500 sccm, and (4) Ar purge for 7.0 s

2.3. Characterization of In_2O_3 TFT and Al_2O_3 film

The electrical properties of TFTs, including their transfer and output characteristics, were measured using a semiconductor parameter analyzer (HP4156A) under dark conditions. To evaluate the stability of the TFTs, a positive bias temperature stress (PBTS) test was conducted by applying a 1 MV/cm field to the gate electrode for 1 h at 60 °C in darkness. Additionally, a constant current stress (CCS) test was conducted by applying 2 and 2.5 V biases to the gate and drain electrodes, respectively, for 1 h at room temperature. Transmission electron microscopy (TEM) images of the fabricated TFTs were captured using a JEM-ARM200F instrument. The crystallinity and density of the channels were analyzed using X-ray diffraction (XRD) and X-ray reflectometry (XRR) with a SmartLab system, respectively. X-ray photoelectron spectroscopy (XPS) was performed using a K-alpha+ instrument to investigate the binding states of In_2O_3 to different Al_2O_3 GIs. Secondary ion mass spectrometry (SIMS) analysis of the In_2O_3/Al_2O_3 layer stack was conducted using an IMS-7f (CAMECA) after annealing under the same conditions as the TFTs to compare the hydrogen-related components of each layer. Owing to the challenges of analyzing secondary ions from a 5-nm-thick film, the thickness of analyzed In_2O_3 was increased to 20 nm. For a more precise assessment of hydrogen concentration, elastic recoil detection (ERD) analysis was performed using an NFC model. Photo-induced current transient spectroscopy (PICTS) analysis was conducted by irradiating a UV-LED with a wavelength of 420 nm at temperatures ranging from −170 to −150 °C to quantitatively analyze the defect states as a function of energy level in the channel.

3. Results and discussion

The electrical characteristics of the four fabricated devices varied depending on the subcyclic ratio of the Al_2O_3 GI, as depicted in Fig. 1 (c–f). A drain voltage (V_D) of 0.1 and 4.1 V was applied to the TFTs, and all devices demonstrated typical on/off characteristics within the gate voltage (V_G) range after annealing at 310 °C. In their as-fabricated state, the devices exhibited comparable performances. However, at higher annealing temperatures, the devices rapidly lost their on/off characteristics. Fig. S1 presents a comprehensive summary of the device characteristics as a function of annealing temperature. Notably, as the subcyclic ratio of T-Al_2O_3 in the GI increased, the turn on voltage (V_{on}) gradually shifted to more negative values, and significantly shifted from −0.85 to −2.8 V in the T1P4 device. In TFTs where the subcyclic ratio of T-Al_2O_3 exceeded that of the T1P4 GI, V_{on} shifted beyond the V_G sweep range, resulting in a conductor-like state (Fig. S2(a)). Field-effect mobility (μ_{FE}) is another critical performance parameter. μ_{FE} remarkably increased from 74.5 to 129.2 cm^2/Vs in the T1P19 device, where super-cycled Al_2O_3 was first introduced, and further increased to 159.3 cm^2/Vs with an increasing subcyclic ratio of T-Al_2O_3. The phenomenon that causes the rapid change in mobility need to be identified along with the V_{on} depending on the subcyclic ratio of the GI. A plausible explanation involves hydrogen diffusion from various GIs during the Al_2O_3 deposition or post-annealing. T-Al_2O_3, which incorporates a significant amount of hydrogen from its H_2O reactant, can help demonstrate the dual role of hydrogen as a defect passivator and a shallow donor in the oxide semiconductors [22,23]. This dual functionality can enhance the mobility by: 1) increasing the carrier concentration through electron donation, which leverages the unique percolation conduction mechanism of oxide semiconductors [34], and 2) passivating electron trap sites, thereby reducing barriers to electron flow and improving overall conductivity [35]. The V_{on} characteristic is highly dependent on the carrier concentration and the gate oxide capacitance (C_{ox}) [36], which tends to shift negatively with an increase in carrier concentration. The capacitance of the all four 30-nm-thick Al_2O_3 GIs, measured using MIM structures, was approximately 0.22 μF/cm^2. Consequently, the variations in V_{on} across the fabricated TFTs are possibly because of the changes in carrier concentration. The graph illustrating the μ_{FE} and V_{on} properties dependent on different Al_2O_3 GIs can be found in Fig. S2(b). A significant increase was observed in the mobility of the T1P19 device, whereas the V_{on} value remained almost unchanged, suggesting that the hydrogen diffused from the GI primarily served as a defect passivator rather than as an electron donor. Furthermore, the introduction of super-cycled Al_2O_3 as a GI can minimize the extrinsic defects caused by oxygen plasma during the PE-Al_2O_3 deposition process. As a result, hysteresis also significantly reduced upon the introduction of the super-cycle. Hysteresis primarily arises from charge trapping process at the interface between the semiconductor and GI or within the GI itself. During the forward and reverse V_G sweeps, these traps can capture charges, leading to a lagging effect in the current-voltage relationship. The extent of hysteresis is closely correlated with the density of defects, and it can manifest across multiple measurement processes. Furthermore, the notable shift in the V_{on} value in the T1P4 device can be attributed to the hydrogen acting more substantially as an electron donor, with increased hydrogen diffusion, significantly affecting V_{on}. Therefore, the influence of the differences in hydrogen diffusion on the electrical characteristics need to be analyzed. Twelve distinct TFTs were measured from each fabricated device and their detailed electrical characteristics are summarized in Table 1, utilizing the following equations:

$$\mu_{FE} = \frac{g_m}{W/L \times C_{ox} \times V_D} \left(g_m \equiv \frac{\partial I_D}{\partial V_G} \right), \quad (1)$$

$$V_{on} = V_G \, (@I_D = 10\, pA \times W/L), \quad (2)$$

where W and L represent the width and length of the TFT channel, extracted using optical microscopy (Fig. S3) and transmission line method (TLM). The V_D was applied at 0.1 V and C_{ox} denotes the capacitance per unit area of GI (Fig. S4(a)). The V_{on} was defined as a practical parameter to evaluate and compare the switching characteristics of TFTs in display application. Overall, no significant differences were observed in the density of Al_2O_3 (Fig. S4(b)). Furthermore, with a leakage current level about 10^{-8} A/cm^2 and a breakdown voltage around 10 MV/cm (Fig. S4(c)), the 30-nm-thick Al_2O_3 proved sufficient as an electrical insulator. Considering the negligible differences in electrical properties and densities of GIs, it can be concluded that general insulating films were successfully grown despite varying the oxygen reactant. The T1P9 device exhibited satisfactory electrical characteristics with a V_{on} of −0.85 V and mobility of 148.1 cm^2/Vs. In contrast, the T1P4 device with a higher proportion of T-Al_2O_3 displayed a significantly negative shift in V_{on}, whereas the T1P19 device with a lower proportion of T-Al_2O_3 exhibited lower mobility and larger hysteresis. The output curves in Fig. S5 indicates that, similar to the transfer curves, a higher drain current was observed as the subcyclic ratio of T-Al_2O_3 in the GI increased, and also demonstrated good contact resistance.

The variations in the electrical characteristics across different devices are hypothesized to be caused by the variations in hydrogen diffusion from the GI. Since the electrical characteristics of the oxide semiconductors are greatly affected by their crystallinity and grain boundaries [37], TEM images and XRD patterns of the TFT channel layer after post-annealing were analyzed to assess potential differences related to the GI process or hydrogen incorporation. In_2O_3 deposited by ALD typically appears in a nanocrystalline state, featuring numerous incomplete bonds at grain boundaries, which introduces more defects compared to the amorphous state [38]. Additionally, the weak oxygen binding energy of indium leads to a high density of oxygen vacancies [9]. TEM analysis (Fig. 2(a-d)) revealed multiple grains within the channel layer, indicating that the presence of numerous grain boundaries. The poly-crystalline nature of In_2O_3 films was consistent across all devices, regardless of the Al_2O_3 subcyclic ratio, requiring further investigation through XRD analysis. The XRD patterns (Fig. 2(e-h)) displayed high intensities in various crystal planes corresponding to the bixbyite structure typical of In_2O_3 (ICDD No. 00–006–0416). This confirms the polycrystalline nature of the films and the presence of multiple grain boundaries, as corroborated by the TEM findings. The similarity in crystal structures across different devices, irrespective of the GI super-cycle type, was further verified; and the planes observed in XRD peaks were matched with those identified in the TEM images using a fast Fourier transform (FFT). The as-deposited In_2O_3 channel layer also exhibited a poly-crystalline state with slightly lower XRD peak intensity as compared to the annealed films (Fig. S6). Given these observations, it is crucial to mitigate the impact of the numerous defects in In_2O_3 through hydrogen passivation to effectively utilize its high mobility as a channel layer in TFTs.

Table 1
Electrical characteristics of TFTs utilizing different Al_2O_3 GIs, presented with their averages and standard deviations.

Device (T-Al_2O_3 Subcycle Proportion)	μ_{FE} [cm^2/Vs]	V_{on} [V]	Hysteresis [V]	Subthreshold Swing [V/dec]
T0P1 (0 %)	74.49 ± 5.94	−0.49 ± 0.12	0.41 ± 0.12	0.16 ± 0.01
T1P19 (5 %)	129.20 ± 3.58	−0.75 ± 0.26	0.22 ± 0.04	0.14 ± 0.01
T1P9 (10 %)	148.12 ± 5.57	−0.85 ± 0.09	0.16 ± 0.05	0.16 ± 0.01
T1P4 (20 %)	159.29 ± 4.11	−2.80 ± 0.24	0.05 ± 0.06	0.21 ± 0.01

To compare the inherent hydrogen content in super-cycled Al_2O_3 and the amount of hydrogen diffused into In_2O_3 from the GI, we performed a SIMS depth profile analysis. The hydrogen in oxide semiconductors can exist in various forms, such as interstitial hydrogen bonded to oxygen or metal atoms, and hydrogen occupying oxygen vacancy sites [39,40]. SIMS detects the mass of emitted secondary ions and identifies all hydrogen species present in these forms. For the purpose of the analysis, hydrogen and hydroxyl group (OH), which can act as electron donors, were investigated. However, strong ion collisions during SIMS analysis can lead to profile tailing, which complicates the comparison of profiles between samples, especially when the samples are fabricated with an actual channel thickness of 5 nm [41]. To mitigate this issue, samples were fabricated with a 20-nm-thick In_2O_3 layer, focusing on analyzing the 5 nm depth in contact with Al_2O_3. The analysis revealed that the introduction of the GI super-cycle increased the hydrogen incorporation, enhancing device performance through precise control of hydrogen content in Al_2O_3. As illustrated in Fig. 3(a), the T1P4 device demonstrated the highest hydrogen intensity at approximately 5 nm depth at the interface between the GI and the active layer, with minor differences observed in other devices. In devices prior to T1P4, hydrogen might predominantly function as an oxygen vacancy passivator rather than existing as interstitial hydrogen, resulting in relatively lower hydrogen intensity levels in SIMS measurements. This passivation led to improvements in mobility by reducing defect states. In contrast, in the T1P4 device, a substantial portion of hydrogen was present as interstitial hydrogen, directly contributing to electron donation. This transition resulted in a notable increase in hydrogen intensity and a marked rise in carrier concentration, which in turn caused a pronounced shift in V_{on} in the T1P4 device. Given that most differences in the amount of diffused hydrogen originated from varying Al_2O_3 designs, the precise hydrogen concentrations in T0P1 and T1P4 Al_2O_3 were further investigated through the ERD analysis, as depicted in Fig. 3(c-d). As presented in Fig. S7, the ERD analysis results for each Al_2O_3 GI demonstrated a gradual increase in hydrogen content with a rising ratio of T-Al_2O_3, which aligns with the expectations. Despite the minor variations in hydrogen concentration from T1P4 to T0P1 Al_2O_3 samples, significant variations were observed in device characteristics. This demonstrates the sensitivity of oxide semiconductor properties to even marginal fluctuations in the hydrogen levels, thereby emphasizing the benefits of precise hydrogen concentration control through the super-cycle method. Additionally, SIMS analysis of OH intensity, illustrated in Fig. 3(b), revealed differences near the interface. Direct comparison of the OH intensities at the Al_2O_3 interface may be challenging owing to fluctuations attributed to the SIMS matrix effect, which compromises the reliability of measurement in this region [42,43]. However, within the depth corresponding to the channel layer thickness, the OH intensities exhibit consistent trends, providing a more reliable basis for analysis. The channel layer of the T0P1 device exhibited the lowest OH intensity, with progressively higher intensities in the T1P19 and T1P9 devices, and the highest intensity in the T1P4 channel layer. These findings, in conjunction with transfer characteristics, indicated that the observed mobility enhancements were predominantly driven by defect passivation, specifically through the passivation of oxygen dangling bonds and interstitial oxygen, leading to the formation of OH groups [39]. The increasement in OH concentration correlated with defect passivation mechanism, as evidenced by the observed trend in electrical characteristics, thus substantiating the role of defect passivation in mobility improvements. Consistently, SIMS results confirmed that the Al_2O_3 super-cycle process enables the precise modulation and controlled diffusion of hydrogen, further aligning with the interpretation of the

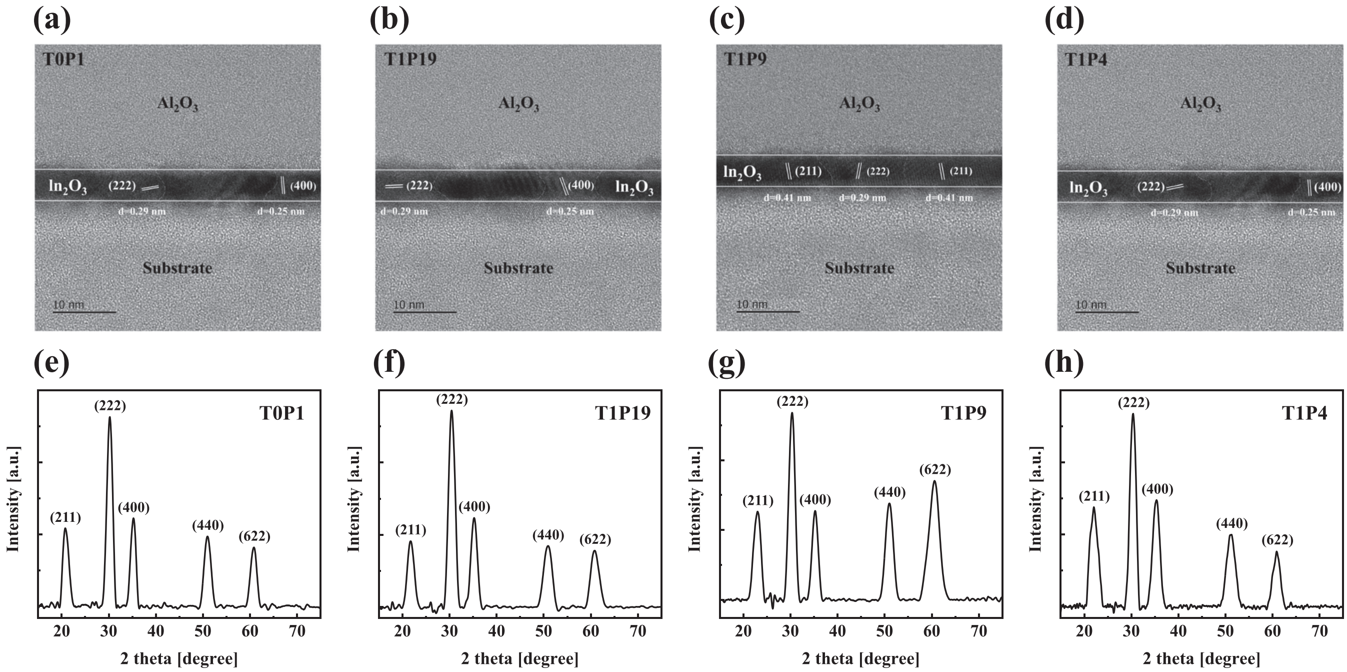

Fig. 2. (a-d) TEM images of each TFT channel cross-section along with crystal planes obtained via FFT analysis, and (e-h) XRD patterns of respective TFT channels.

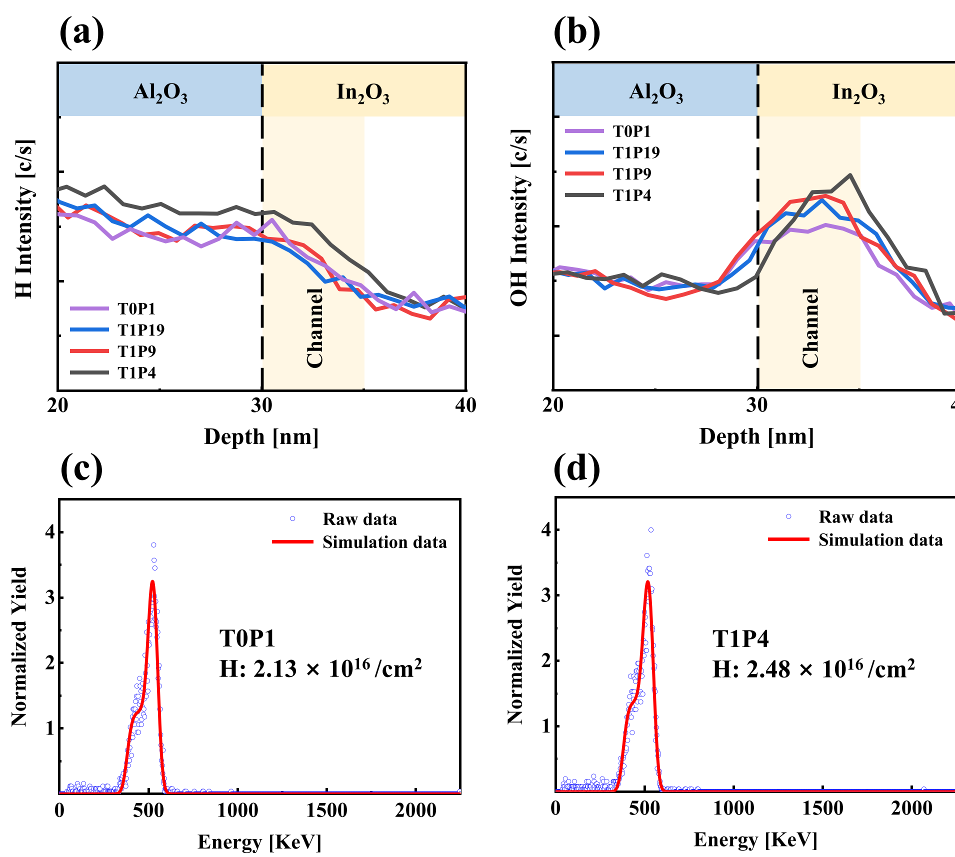

Fig. 3. SIMS depth profiles of (a) H and (b) OH in Al_2O_3/In_2O_3 stacks mimicking each TFT device. Normalized yield of detected H in (c) T0P1 and (d) T1P4 Al_2O_3 films quantitatively analyzed by ERD.

electrical properties.

XPS analysis was conducted to investigate changes in the oxygen binding state of In_2O_3 in relation to variations in the subcyclic ratio of Al_2O_3. This analysis is crucial because the properties of oxide semiconductors are closely associated with their oxygen binding states [44]. To replicate the environment of the fabricated devices, XPS samples were prepared by depositing super-cycled Al_2O_3 on a 5-nm-thick In_2O_3, and the O 1*s* peak near the In_2O_3 surface was analyzed through a depth profile. As depicted in Fig. 4, the O 1 *s* peak around 530 eV was deconvoluted into three distinct subpeaks: (1) the metal-oxygen bond (M-O) at 530.2 eV, (2) the oxygen deficient bond at 531.1 eV, and (3) the oxygen-hydrogen bond (-OH) at 532.5 eV [24]. The proportions of each oxygen-related bond were evaluated based on the area of each subpeak and summarized in Table 2. The proportion of subpeaks related to oxygen deficiency was notably high about 34.16 % in the channel layer of the T0P1 device; however, as the subcyclic ratio of T-Al_2O_3 increased, this proportion gradually decreased to 23.29 %. In particular, the ratio of oxygen deficient bonds changed significantly with the presence of T-Al_2O_3. Other studies using simulations have demonstrated that hydrogen in oxide semiconductors tends to occupy vacant sites ($H_i^+ + V_O \rightarrow H_O^+$) [39]. Although oxygen plasma exposure during deposition had the potential to saturate some oxygen vacancies, the high plasma power also tended to generate additional vacancies by causing structural damage [45]. In this study, with Al_2O_3 deposited at a plasma power of 100 W, observing that a lower ratio of PE-Al_2O_3 was associated with fewer oxygen deficiencies. This suggests that reducing the proportion of PE-Al_2O_3 in the cycle sequence mitigates plasma-induced damage, thereby enhancing electron mobility by reducing electron trapping and scattering. Moreover, the OH peak portion increased from approximately 3.73 % in the T0P1 device channel to 8.22 % in the T1P4 device channel as the subcyclic ratio of T-Al_2O_3 increased. In oxide semiconductors, oxygen interstitials (O_i) also serve as electron trap sites, and hydrogen passivates these interstitials, increasing the OH component through the reaction $H^+ + O_i^{2-} \rightarrow OH + e^-$ [46]. The formation of OH can also release electrons, leading to a higher carrier concentration and affecting the electrical properties of devices. Overall, an increase in the subcyclic ratio of T-Al_2O_3 in super-cycle facilitated hydrogen diffusion into In_2O_3, which effectively served the dual roles of defect passivator and electron donor. The rapid decrease in oxygen-deficient defects following the introduction of super-cycle GI and the increase in carrier concentration with higher subcyclic ratios of T-Al_2O_3 determined the mobility and V_{on} values observed in the transfer characteristics.

The PICTS analysis was conducted to quantitatively assess the defect states within the In_2O_3 channel layers. By applying a positive gate bias and UV illumination to TFTs, optically excited electrons become trapped in defects and are subsequently re-emitted, generating a transient current [47,48]. By measuring this current, the defect concentrations corresponding to different energy levels were extracted. Owing to the fundamental principles and measurement methodology of PICTS, obtaining the state density across continuous energy levels is challenging. Instead, this technique allows for the extraction of state densities at discrete energy levels. Furthermore, as PICTS relies on photocurrent, it is less sensitive to localized tail states, enabling a more precise comparison of state variations induced by hydrogen that affect TFT operation. Fig. 5 illustrates the shallow level state densities at various energy levels in the In_2O_3 channel adjacent to the different Al_2O_3 GIs, while Table 3 summarizes the shallow level state density values by their activation energy and the total densities for each device. The results indicated that as the hydrogen content in the GI increased, the total number of shallow states within 0.2 eV of the conduction band minimum (CBM) of increased. Hydrogen plays a pivotal role in the formation of shallow states by passivating oxygen vacancies or structural defects such as dangling bonds, as well as existing in forms of weakly bonded hydrogen species, including M-OH [39,49–51]. These interactions contribute to lattice stabilization, mitigate carrier scattering, and facilitate the generation of free carriers, thereby enhancing mobility and device stability. PICTS results demonstrated an increase in shallow states from T0P1 to T1P9 channels, with only a minor rise in T1P4, indicating that hydrogen primarily supported passivation corroborating up to this threshold. However, as the hydrogen content exceeded a certain threshold, hydrogen increasingly accumulated as interstitials rather than exclusively passivating structural defects. This interstitial hydrogen significantly contributed to free carrier concentration, resulting in a noticeable shift in V_{on} and an increase in carrier density, particularly in the T1P4 device, as verified by SIMS analysis. Consequently, it can be concluded that hydrogen controlled via super-cycled Al_2O_3 GIs effectively passivates the oxygen-related defects in the oxide semiconductor, and excess hydrogen introduces additional carriers, corroborating prior analyses.

The intrinsic defects in In_2O_3 can negatively affect the stability of

Table 2
Proportions of oxygen-related bonds in the active layer with different Al_2O_3 GIs.

Device	M-O	Oxygen Deficiency	-OH
T0P1	62.11	34.16	3.73
T1P19	67.11	28.19	4.70
T1P9	67.57	26.35	6.08
T1P4	68.49	23.29	8.22

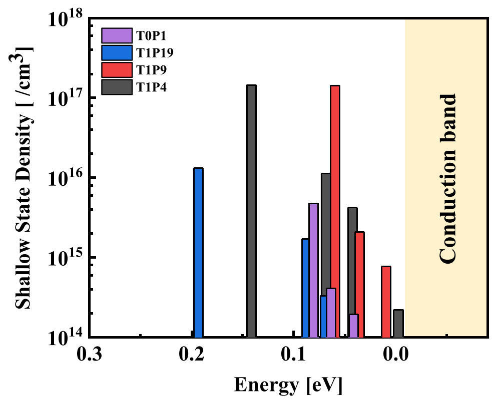

Fig. 5. Distribution of shallow level states in the TFT channel layers with different Al_2O_3 GIs.

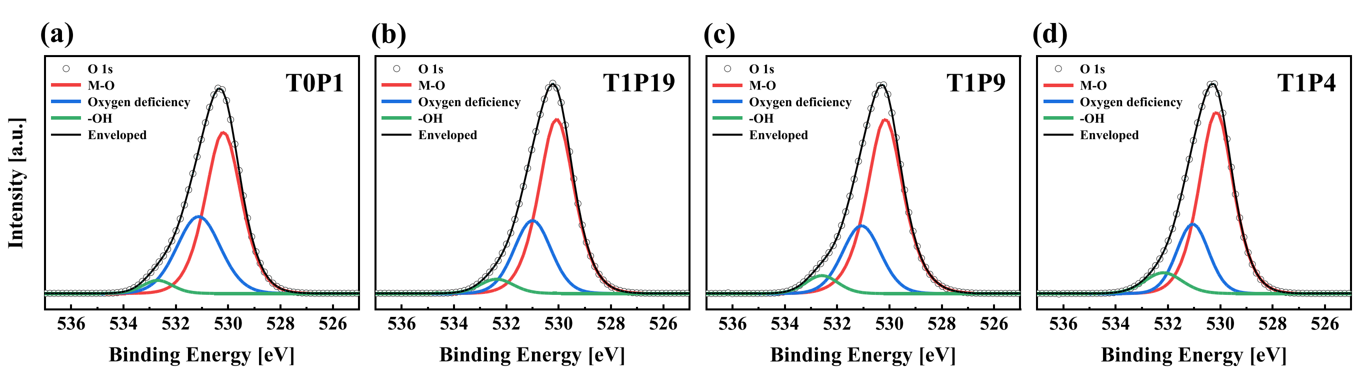

Fig. 4. Deconvoluted XPS O 1 s spectra of In_2O_3 films deposited with the same sequence for (a) T0P1, (b) T1P19, (c) T1P9, and (d) T1P4 channel layers.

Table 3
Summary of shallow level state densities and total densities within 0.2 eV of CBM by activation energy quantitatively extracted through PICTS analysis.

Device	T0P1		T1P19		T1P9		T1P4	
	E_a [eV]	N_d [/cm^3]	E_a [eV]	N_d [/cm^3]	E_a [eV]	N_d [/cm^3]	E_a [eV]	N_d [/cm^3]
Shallow Level States	0.028	1.93×10^{14}	0.056	3.28×10^{14}	0.014	7.68×10^{14}	0.011	2.21×10^{14}
	0.050	4.09×10^{14}	0.083	1.70×10^{15}	0.040	2.07×10^{15}	0.056	4.20×10^{15}
	0.067	4.76×10^{14}	-		0.064	1.42×10^{17}	0.089	1.12×10^{16}
	-		0.189	1.31×10^{16}	-		0.155	1.45×10^{17}
Total Density [/cm^3]	5.36×10^{15}		1.51×10^{16}		1.45×10^{17}		1.60×10^{17}	

TFTs. Additionally, extrinsic defects, such as charge trapping centers (M-O-O) at the semiconductor/GI interface may be introduced during the PE-Al_2O_3 deposition process by oxygen plasma [32,45]. Therefore, the stability of the TFTs is significantly influenced by the subcyclic ratio of T-Al_2O_3. To assess electrical stability, variations in the V_{on} under PBTS condition were monitored by applying a bias of 1 MV/cm at 60 °C for 1 hour [52,53]. The transfer curves illustrating these changes for each device are depicted in Fig. 6. The mechanism driving V_{on} shift in PBTS can be attributed to the electrons trapped at defect sites at both within the active layer and the active/GI interface when a positive gate bias is applied to the gate electrode [54]. Thus, an increase in defects at the active layer or interface leads to a larger positive shift in V_{on}. As depicted in Fig. 6(a-d), increasing hydrogen content in super-cycled Al_2O_3 improved the PBTS stability, with the V_{on} shift decreasing from 1.57 to 0.35 V after 1 h. This improvement is attributed to hydrogen passivating of bulk defects within In_2O_3, effectively targeting structural imperfections such as dangling bonds and electron trap sites, including interstitial oxygen [55]. Similarly, improved reliability in In_2O_3 TFTs has been achieved by mitigating oxygen vacancies and reducing defect densities [56]. Furthermore, reducing the number of PE-Al_2O_3 cycles minimized the formation of interface defects by limiting plasma exposure duration. This combination of bulk defect passivation by hydrogen and minimized plasma-induced interface defect via optimized PE-Al_2O_3 cycles collectively contributed to the overall enhancement in device stability. However, an excessive proportion of T-Al_2O_3 resulted in a further negative shift in V_{on}, highlighting the need to optimize the subcyclic ratio. Although the PBTS performance did not vary substantially between the T1P9 and T1P4 configurations, a notable difference in V_{on} was observed. Consequently, the T1P9 device demonstrated an optimal balance between the stability and electrical performance. Furthermore, no significant differences were observed in the stability negative bias temperature stress (NBTS) and negative bias illumination stress (NBIS), as depicted in Fig. S8. The negligible V_{on} degradations under NBTS and NBIS suggest that hydrogen incorporation did not cause any stability degradation under negative voltages. Comparative data on the electrical performance and PBTS stability of TFTs using In_2O_3 from the literature are summarized in Table S1. As compared to extant In_2O_3-based TFTs, our device demonstrated superior electrical performance, as well as competitive reliability.

The CCS stability was assessed by monitoring the decline in on-current during TFT operation, which is essential for determining the duration that brightness remains consistent under the stress exerted by the light-emitting device of the display. The change in on-current change was evaluated by subjecting each device to gate and drain bias stresses for 1 h. The normalized current over time is illustrated in Fig. 7. During the CCS analysis, with the device in the on state, charges were trapped by defects at the GI/active interface. This trapping led to a gradual decrease in current owing to the gate voltage screening effect caused by the trapped charges. The decay in drain current was fitted using a stretched exponential equation:

$$\frac{I_D(t)}{I_D(0)} = \exp\left\{-(t/\tau)^{\beta}\right\}, \tag{3}$$

where $I_D(t)$ denotes the drain current at time t, τ represents characteristic time related to the charge mobile state, and β indicates a dispersion parameter related to the localized energy states [57,58]. The T1P4 device, with the highest T-Al_2O_3 subcyclic ratio, demonstrated a high retention rate of approximately 98.7 % after 1 h, with progressively lower retention rates of 93.6 %, 86.6 %, and 71.3 % observed in devices with decreasing T-Al_2O_3 content. The τ parameter from the stretched exponential equation in Table 4, indicative of the mobile state time of

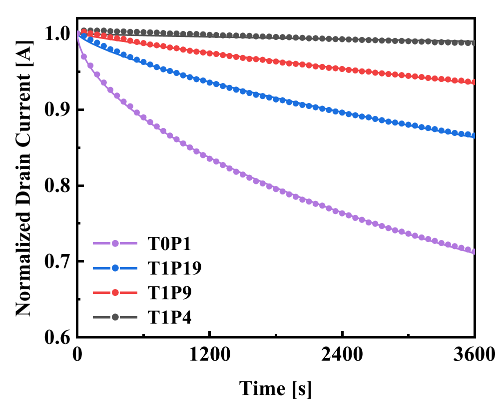

Fig. 7. Decline in normalized drain current and fitted graphs over time under CCS.

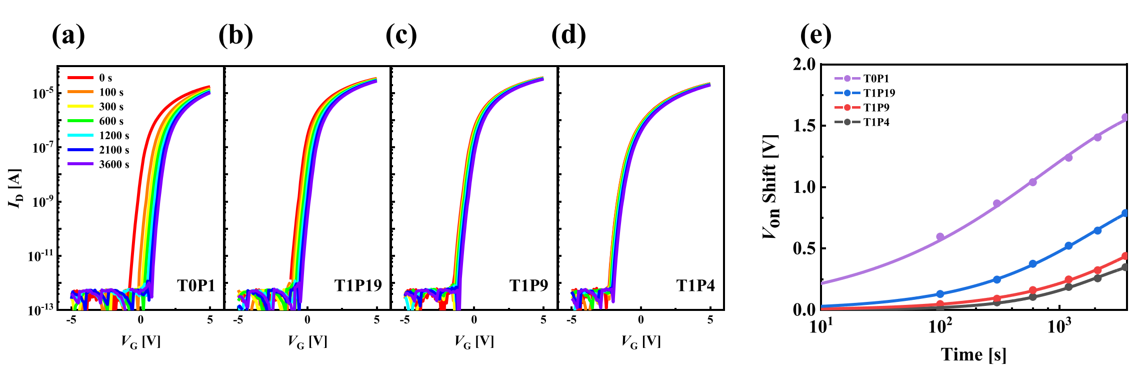

Fig. 6. Shifts in the transfer curves under PBTS conditions for (a) T0P1, (b) T1P19, (c) T1P9, and (d) T1P4 devices, and (e) the graph illustrating V_{on} shifts over time.

Table 4
Parameters of stretched exponential equation extracted from the CCS stability measurement.

Device	T1P0	T1P19	T1P9	T1P4
τ [s]	1.58×10^4	4.96×10^4	1.08×10^5	1.11×10^5
β	0.70	0.73	0.80	0.80

the charge, also displayed an increase. This trend aligns with the previously observed PBTS stability results, suggesting that hydrogen diffusion from Al_2O_3 to In_2O_3 significantly influences defect passivation by reducing the number of trap sites. Among all tested devices, the T1P9 device exhibited the best overall performance. It incorporated an optimal amount of hydrogen into the semiconductor, effectively passivated defects, and maintained a moderate carrier concentration, thereby preventing shifts in V_{on}. The Al_2O_3 super-cycle method is not only applicable to In_2O_3 TFTs but also enables precise control over hydrogen diffusion into the semiconductor by adjusting the GI subcyclic ratio. Consequently, this super-cycle method, when used with different oxygen reactants, can be adapted to various oxide semiconductors for realizing excellent performance with each oxide semiconductor.

4. Conclusions

In this study, we successfully fabricated high-performance In_2O_3 TFTs by controlling hydrogen diffusion from an Al_2O_3 dielectric film into the active layer using a novel ALD super-cycle method. By utilizing both H_2O and O_2 plasma as oxygen reactants in the deposition of the Al_2O_3 film, we achieved precise regulation of the hydrogen content. The transfer characteristics of the In_2O_3 TFTs varied with the amount of hydrogen diffused from the T-Al_2O_3 of GI into the active layer. The SIMS and ERD analyses confirmed that hydrogen successfully played a dual role in donating electrons and passivating defects with the variation in hydrogen. Initially, hydrogen diffusion effectively passivated the defects in In_2O_3; however, excessive hydrogen led to increased carrier concentration, which potentially compromised the transistor functionality. XRD and TEM analyses revealed that the polycrystalline nature of In_2O_3 introduced numerous grain boundary defects. The XPS results confirmed the effective passivation of defects, such as dangling bonds, by hydrogen. PICTS analysis quantitatively assessed the shallow state densities and identified the optimal hydrogen concentration required to effectively passivate the majority of defects while maintaining an appropriate carrier concentration. PBTS and CCS stability tests demonstrated that hydrogen passivation significantly enhanced device stability, highlighting the potential of these TFTs for display applications. Among the devices tested, the T1P9 device exhibited the best performance, with effective defect passivation and an optimal carrier concentration, resulting in a high mobility of 148.12 cm^2/Vs, moderate V_{on} of −0.85 V, and V_{on} shift of 0.44 V under PBTS condition. Although the T1P9 device achieved the best performance among the In_2O_3 TFTs, precise hydrogen control in Al_2O_3 remains crucial for optimizing various oxide semiconductors. This study introduced a novel methodology for extremely precise hydrogen incorporation, which is vital for the development of devices with exceptionally high mobility.

CRediT authorship contribution statement

Ko Jong Beom: Writing – review & editing, Supervision, Methodology, Investigation, Data curation. **Chung Kwun-Bum:** Writing – review & editing, Resources, Data curation. **Park Sang-Hee Ko:** Writing – review & editing, Supervision, Resources, Project administration, Funding acquisition. **Shin Dong Yeob:** Investigation, Data curation. **Kim Hwa Young:** Writing – review & editing, Writing – original draft, Visualization, Validation, Methodology, Investigation, Formal analysis, Data curation. **Cho Seong-In:** Writing – review & editing, Investigation, Data curation, Conceptualization.

Declaration of Competing Interest

The authors declare that they have no known competing financial interests or personal relationships that could have appeared to influence the work reported in this paper.

Acknowledgements

This work was supported by Technology Innovation Program [Project Number: 20016319] funded by the Ministry of Trade, Industry and Energy (MOTIE, Korea); the National Research Foundation of Korea (NRF) [Grant Number: RS-2023-00236421] funded by the Ministry of Science & ICT (MSIT); and the Research Fund of Hanbat National University in 2024.

Appendix A. Supporting information

Supplementary data associated with this article can be found in the online version at doi:10.1016/j.jallcom.2025.179353.

Data availability

Data will be made available on request.

References

[1] J.S. Park, W.J. Maeng, H.S. Kim, J.S. Park, Review of recent developments in amorphous oxide semiconductor thin-film transistor devices, Thin Solid Films 520 (2012) 1679–1693, https://doi.org/10.1016/j.tsf.2011.07.018.
[2] T. Kim, C.H. Choi, J.S. Hur, D. Ha, B.J. Kuh, Y. Kim, M.H. Cho, S. Kim, J.K. Jeong, Progress, challenges, and opportunities in oxide semiconductor devices: a key building block for applications ranging from display backplanes to 3D integrated semiconductor chips, Adv. Mater. 35 (2023) e2204663, https://doi.org/10.1002/adma.202204663.
[3] H.J. Kim, J.H. Lee, Highly sensitive and selective gas sensors using p-type oxide semiconductors: overview, Sens. Actuator B Chem. 192 (2014) 607–627, https://doi.org/10.1016/j.snb.2013.11.005.
[4] T. Iwasaki, N. Itagaki, T. Den, H. Kumomi, K. Nomura, T. Kamiya, H. Hosono, Combinatorial approach to thin-film transistors using multicomponent semiconductor channels: an application to amorphous oxide semiconductors in In–Ga–Zn–O system, Appl. Phys. Lett. 90 (2007), https://doi.org/10.1063/1.2749177.
[5] J. Kim, D.H. Kim, S.-I. Cho, S.H. Lee, W. Jeong, S.-H.K. Park, Channel-shortening effect suppression of a high-mobility self-aligned oxide TFT using trench structure, IEEE Electron Device Lett. 42 (2021) 1798–1801, https://doi.org/10.1109/led.2021.3125146.
[6] K. Nomura, H. Ohta, K. Ueda, T. Kamiya, M. Hirano, H. Hosono, Thin-film transistor fabricated in single-crystalline transparent oxide semiconductor, Science 300 (2003) 1269–1272, https://doi.org/10.1126/science.1083212.
[7] T. Kamiya, K. Nomura, H. Hosono, Origins of high mobility and low operation voltage of amorphous oxide TFTs: electronic structure, electron transport, defects and doping, J. Disp. Technol. 5 (2009) 273–288, https://doi.org/10.1109/Jdt.2009.2021582.
[8] O. Bierwagen, Indium oxide-a transparent, wide-band gap semiconductor for (opto)electronic applications, Semicond. Sci. Technol. 30 (2015), https://doi.org/10.1088/0268-1242/30/2/024001.
[9] H.-J. Oh, Y.-S. Kim, H.-J. Jeong, S. Lee, J.S. Park, J.-S. Park, Compositional tailoring of indium-free GZO layers via plasma-enhanced atomic layer deposition for highly stable IGZO/GZO TFT, J. Inf. Disp. 25 (2023) 295–303, https://doi.org/10.1080/15980316.2023.2292465.
[10] Y. Magari, T. Kataoka, W. Yeh, M. Furuta, High-mobility hydrogenated polycrystalline In2O3 (In2O3:H) thin-film transistors, Nat. Commun. 13 (2022) 1078, https://doi.org/10.1038/s41467-022-28480-9.
[11] S. Jeong, Y.G. Ha, J. Moon, A. Facchetti, T.J. Marks, Role of gallium doping in dramatically lowering amorphous-oxide processing temperatures for solution-derived indium zinc oxide thin-film transistors, Adv. Mater. 22 (2010) 1346–1350, https://doi.org/10.1002/adma.200902450.
[12] W.F. Zhang, Z.B. He, G.D. Yuan, J.S. Jie, L.B. Luo, X.J. Zhang, Z.H. Chen, C.S. Lee, W.J. Zhang, S.T. Lee, High-performance, fully transparent, and flexible zinc-doped indium oxide nanowire transistors, Appl. Phys. Lett. 94 (2009), https://doi.org/10.1063/1.3100194.
[13] A. Sil, L. Avazpour, E.A. Goldfine, Q. Ma, W. Huang, B. Wang, M.J. Bedzyk, J. E. Medvedeva, A. Facchetti, T.J. Marks, Structure–charge transport relationships in fluoride-doped amorphous semiconducting indium oxide: combined experimental and theoretical analysis, Chem. Mat. 32 (2019) 805–820, https://doi.org/10.1021/acs.chemmater.9b04257.

[14] B.K. Yap, Z.H. Zhang, G.S.H. Thien, K.Y. Chan, C.Y. Tan, Recent advances of In2O3-based thin-film transistors: a review, Appl. Surf. Sci. Adv. 16 (2023), https://doi.org/10.1016/j.apsadv.2023.100423.
[15] S.M. George, Atomic layer deposition: an overview, Chem. Rev. 110 (2010) 111–131, https://doi.org/10.1021/cr900056b.
[16] D.G. Kim, H. Choi, Y.S. Kim, D.H. Lee, H.J. Oh, J.H. Lee, J. Kim, S. Lee, B. Kuh, T. Kim, H.Y. Kim, J.S. Park, Selectively nitrogen doped ALD-IGZO TFTs with extremely high mobility and reliability, ACS Appl. Mater. Interfaces 15 (2023) 31652–31663, https://doi.org/10.1021/acsami.3c05678.
[17] J. Sheng, T. Hong, D. Kang, Y. Yi, J.H. Lim, J.S. Park, Design of InZnSnO semiconductor alloys synthesized by supercycle atomic layer deposition and their rollable applications, ACS Appl. Mater. Interfaces 11 (2019) 12683–12692, https://doi.org/10.1021/acsami.9b02999.
[18] N. Woo, S.I. Cho, S.H.K. Park, Optimal aluminum doping method in PEALD for designing outstandingly stable InAlZnO TFT, Adv. Mater. Interfaces 10 (2023), https://doi.org/10.1002/admi.202300128.
[19] C.S. Hwang, S.H.K. Park, H. Oh, M.K. Ryu, K.I. Cho, S.M. Yoon, Vertical channel ZnO thin-film transistors using an atomic layer deposition method, IEEE Electron Device Lett. 35 (2014) 360–362, https://doi.org/10.1109/Led.2013.2296604.
[20] C.H. Wu, H.H. Hsieh, C.W. Chien, C.C. Wu, Self-aligned top-gate coplanar In-Ga-Zn-O thin-film transistors, J. Disp. Technol. 5 (2009) 515–519, https://doi.org/10.1109/Jdt.2009.2026189.
[21] M.H. Kim, J.W. Park, J.H. Lim, D.K. Choi, The effect of hydrogen on the device stability of amorphous InGaZnO thin-film transistors under positive bias with various temperature stresses, Phys. Status Solidi A Appl. Mater. 216 (2019), https://doi.org/10.1002/pssa.201900297.
[22] Y. Hanyu, K. Domen, K. Nomura, H. Hiramatsu, H. Kumomi, H. Hosono, T. Kamiya, Hydrogen passivation of electron trap in amorphous In-Ga-Zn-O thin-film transistors, Appl. Phys. Lett. 103 (2013), https://doi.org/10.1063/1.4832076.
[23] H.Y. Noh, J. Kim, J.S. Kim, M.J. Lee, H.J. Lee, Role of hydrogen in active layer of oxide-semiconductor-based thin film transistors, Crystals 9 (2019) 75, https://doi.org/10.3390/cryst9020075.
[24] J.B. Ko, S.H. Lee, K.W. Park, S.K. Park, Interface tailoring through the supply of optimized oxygen and hydrogen to semiconductors for highly stable top-gate-structured high-mobility oxide thin-film transistors, RSC Adv. 9 (2019) 36293–36300, https://doi.org/10.1039/c9ra06960g.
[25] R. Kamal, P. Chandravanshi, D.K. Choi, S.M. Bobade, The effect of annealing in forming gas on the a-IGZO thin film transistor performance and valence band cut-off of IGZO on SiNx, Curr. Appl. Phys. 15 (2015) 648–653, https://doi.org/10.1016/j.cap.2015.02.017.
[26] B. Du Ahn, H.S. Shin, H.J. Kim, J.-S. Park, J.K. Jeong, Comparison of the effects of Ar and H2 plasmas on the performance of homojunctioned amorphous indium gallium zinc oxide thin film transistors, Appl. Phys. Lett. 93 (2008), https://doi.org/10.1063/1.3028340.
[27] J.B. Ko, S.I. Cho, S.K. Park, Engineering a subnanometer interface tailoring layer for precise hydrogen incorporation and defect passivation for high-end oxide thin-film transistors, ACS Appl. Mater. Interfaces 15 (2023) 47799–47809, https://doi.org/10.1021/acsami.3c10185.
[28] S.I. Cho, N. Woo, H.J. Jeong, S.H.K. Park, Inserting interfacial layer for atomic-scaled hydrogen control to enhance electrical properties of InZnO TFTs, IEEE Electron Device Lett. 44 (2023) 650–653, https://doi.org/10.1109/Led.2023.3250439.
[29] M. Kot, C. Das, Z. Wang, K. Henkel, Z. Rouissi, K. Wojciechowski, H.J. Snaith, D. Schmeisser, Room-temperature atomic layer deposition of Al2O3: impact on efficiency, stability and surface properties in perovskite solar cells, ChemSusChem 9 (2016) 3401–3406, https://doi.org/10.1002/cssc.201601186.
[30] J. Van Hemmen, S. Heil, J. Klootwijk, F. Roozeboom, C. Hodson, M. Van de Sanden, W. Kessels, Plasma and thermal ALD of Al2O3 in a commercial 200 mm ALD reactor, J. Electrochem. Soc. 154 (2007) G165, https://doi.org/10.1149/1.2737629.
[31] P. Singh, R.K. Jha, R.K. Singh, B.R. Singh, Preparation and characterization of Al2O3 film deposited by RF sputtering and plasma enhanced atomic layer deposition, J. Vac. Sci. Technol. B 36 (2018), https://doi.org/10.1116/1.5023591.
[32] H. Kim, I.K. Oh, Review of plasma-enhanced atomic layer deposition: technical enabler of nanoscale device fabrication, Jpn. J. Appl. Phys. 53 (2014), https://doi.org/10.7567/Jjap.53.03da01.
[33] Y. Im, S.I. Cho, J. Kim, N. Woo, J.B. Ko, S.H.K. Park, Buffer layer engineering of indium oxide based trench TFT for ultra high current driving, IEEE Electron Device Lett. 44 (2023) 1849–1852, https://doi.org/10.1109/Led.2023.3312360.
[34] T. Kamiya, K. Nomura, H. Hosono, Electronic structures above mobility edges in crystalline and amorphous In-Ga-Zn-O: percolation conduction examined by analytical model, J. Disp. Technol. 5 (2009) 462–467, https://doi.org/10.1109/Jdt.2009.2022064.
[35] S. Lee, K. Ghaffarzadeh, A. Nathan, J. Robertson, S. Jeon, C. Kim, I.H. Song, U. I. Chung, Trap-limited and percolation conduction mechanisms in amorphous oxide semiconductor thin film transistors, Appl. Phys. Lett. 98 (2011), https://doi.org/10.1063/1.3589371.
[36] T. Kamiya, K. Nomura, H. Hosono, Present status of amorphous In-Ga-Zn-O thin-film transistors, Sci. Technol. Adv. Mater. 11 (2010) 044305, https://doi.org/10.1088/1468-6996/11/4/044305.
[37] K. Nomura, T. Kamiya, H. Ohta, K. Ueda, M. Hirano, H. Hosono, Carrier transport in transparent oxide semiconductor with intrinsic structural randomness probed using single-crystalline InGaO3(ZnO)5 films, Appl. Phys. Lett. 85 (2004) 1993–1995, https://doi.org/10.1063/1.1788897.
[38] B. Macco, H.C. Knoops, W.M. Kessels, Electron scattering and doping mechanisms in solid-phase-crystallized In2O3:H prepared by atomic layer deposition, ACS Appl. Mater. Interfaces 7 (2015) 16723–16729, https://doi.org/10.1021/acsami.5b04420.
[39] Y. Kang, B.Du Ahn, J.H. Song, Y.G. Mo, H.H. Nahm, S. Han, J.K. Jeong, Hydrogen bistability as the origin of photo-bias-thermal instabilities in amorphous oxide semiconductors, Adv. Electron, Mater. 1 (2015), https://doi.org/10.1002/aelm.201400006.
[40] A. Janotti, C.G. Van de Walle, Hydrogen multicentre bonds, Nat. Mater. 6 (2007) 44–47, https://doi.org/10.1038/nmat1795.
[41] C.W. Magee, R.E. Honig, Depth profiling by SIMS-depth resolution, dynamic-range and sensitivity, Surf. Interface Anal. 4 (1982) 35–41, https://doi.org/10.1002/sia.740040202.
[42] V.R. Deline, W. Katz, C.A. Evans, P. Williams, Mechanism of the SIMS matrix effect, Appl. Phys. Lett. 33 (1978) 832–835, https://doi.org/10.1063/1.90546.
[43] T. Toda, W. Deapeng, J. Jingxin, H. Mai Phi, M. Furuta, Quantitative analysis of the effect of hydrogen diffusion from silicon oxide etch-stopper layer into amorphous In–Ga–Zn–O on thin-film transistor, IEEE Trans. Electron Devices 61 (2014) 3762–3767, https://doi.org/10.1109/ted.2014.2359739.
[44] K. Nomura, T. Kamiya, E. Ikenaga, H. Yanagi, K. Kobayashi, H. Hosono, Depth analysis of subgap electronic states in amorphous oxide semiconductor, a-In-Ga-Zn-O, studied by hard x-ray photoelectron spectroscopy, J. Appl. Phys. 109 (2011), https://doi.org/10.1063/1.3560769.
[45] F. Schöppach, D. Splith, H. von Wenckstern, M. Grundmann, Oxygen plasma treatment to enable indium oxide MESFET devices, Adv. Electron. Mater. 9 (2023) 2300291, https://doi.org/10.1002/aelm.202300291.
[46] S.H. Bae, J.H. Yang, Y.H. Kim, Y.H. Kwon, N.J. Seong, K.J. Choi, C.S. Hwang, S. M. Yoon, Roles of oxygen interstitial defects in atomic-layer deposited InGaZnO thin films with controlling the cationic compositions and gate-stack processes for the devices with subμm channel lengths, ACS Appl. Mater. Interfaces 14 (2022) 31010–31023, https://doi.org/10.1021/acsami.2c07258.
[47] H. Hong, K.S. Jeong, J.H. Lim, K.S. Son, K.B. Chung, Quantitative analysis of defect states in amorphous InGaZnO thin-film transistors using photoinduced current transient spectroscopy, J. Appl. Phys. 130 (2021), https://doi.org/10.1063/5.0050111.
[48] Y.S. Kim, H.Y.M. Hong, T.H.Y. Hong, S.H. Choi, K.B. Chung, J.S. Park, Attaining quantitatively fewer defects in close-packed InGaZnO synthesized using atomic layer deposition, Appl. Surf. Sci. 664 (2024), https://doi.org/10.1016/j.apsusc.2024.160242.
[49] H.H. Nahm, C.H. Park, Y.S. Kim, Bistability of hydrogen in ZnO: origin of doping limit and persistent photoconductivity, Sci. Rep. 4 (2014) 4124, https://doi.org/10.1038/srep04124.
[50] H.-W. Yeon, S.-M. Lim, J.-K. Jung, H. Yoo, Y.-J. Lee, H.-Y. Kang, Y.-J. Park, M. Kim, Y.-C. Joo, Structural-relaxation-driven electron doping of amorphous oxide semiconductors by increasing the concentration of oxygen vacancies in shallow-donor states, NPG Asia Mater. 8 (2016) e250-e250, https://doi.org/10.1038/am.2016.11.
[51] K. Nomura, T. Kamiya, H. Hosono, Effects of diffusion of hydrogen and oxygen on electrical properties of amorphous oxide semiconductor, In-Ga-Zn-O, ECS J. Solid State Sci. Technol. 2 (2012) P5, https://doi.org/10.1149/2.011301jss.
[52] K.S. Yoo, C.-H. Lee, D.-G. Kim, S.-H. Choi, W.-B. Lee, C.-K. Park, J.-S. Park, High mobility and productivity of flexible In2O3 thin-film transistors on polyimide substrates via atmospheric pressure spatial atomic layer deposition, Appl. Surf. Sci. 646 (2024) 158950, https://doi.org/10.1016/j.apsusc.2023.158950.
[53] S.-N. Choi, S.-M. Yoon, Effects of oxidants on the bias-stress instabilities of In-Ga-Zn-O thin film transistors using HfO2 gate insulator prepared by atomic layer deposition, IEEE Electron Device Lett. 41 (2020) 425–428, https://doi.org/10.1109/led.2020.2970751.
[54] A. Suresh, J.F. Muth, Bias stress stability of indium gallium zinc oxide channel based transparent thin film transistors, Appl. Phys. Lett. 92 (2008), https://doi.org/10.1063/1.2824758.
[55] Y. Hanyu, K. Domen, K. Nomura, H. Hiramatsu, H. Kumomi, H. Hosono, T. Kamiya, Hydrogen passivation of electron trap in amorphous In-Ga-Zn-O thin-film transistors, Appl. Phys. Lett. 103 (2013), https://doi.org/10.1063/1.4832076.
[56] J.-Y. Lee, G. Tarsoly, X.-L. Wang, H.-L. Zhao, K.-J. Heo, S.-J. Kim, Engineering a solution-processed In2O3 TFT with improved ambient stability via MoO3 doping, IEEE Trans. Electron Devices 71 (2024) 1946–1950, https://doi.org/10.1109/ted.2024.3360186.
[57] J.M. Lee, I.T. Cho, J.H. Lee, H.I. Kwon, Bias-stress-induced stretched-exponential time dependence of threshold voltage shift in InGaZnO thin film transistors, Appl. Phys. Lett. 93 (2008), https://doi.org/10.1063/1.2977865.
[58] W.H. Lee, S.J. Lee, J.A. Lim, J.H. Cho, Printed In-Ga-Zn-O drop-based thin-film transistors sintered using intensely pulsed white light, RSC Adv. 5 (2015) 78655–78659, https://doi.org/10.1039/c5ra13573g.